catalysts

MDPI

Article

Titanosilicate ETS-10-Modified Cu_2O for Enhanced Visible-Light Photoelectrochemical Activity

Ewelina Szaniawska-Białas [1,2,3], Aleksandra Parzuch [1], Linh Trinh [1], Pavla Eliášová [2] and Renata Solarska [1,*]

[1] Laboratory of Molecular Research for Solar Energy Innovations, Centre of New Technologies, University of Warsaw, Stefana Banacha 2c, 02-097 Warszawa, Poland; ewelina.szaniawska@wat.edu.pl (E.S.-B.); a.parzuch@student.uw.edu.pl (A.P.); l.trinh@cent.uw.edu.pl (L.T.)
[2] Department of Physical and Macromolecular Chemistry, Faculty of Science, Charles University, Hlavova 8, 128 40 Prague, Czech Republic; pavla.eliasova@natur.cuni.cz
[3] Department of Functional Materials and Hydrogen Technology, Faculty of Advanced Technologies and Chemistry, Military University of Technology, 2 Kaliskiego Street, 00-908 Warsaw, Poland
* Correspondence: r.solarska@cent.uw.edu.pl

Abstract: Copper(I) oxide (Cu_2O)-based photocathodes are promising materials for carbon dioxide (CO_2) reduction under visible light due to copper's abundance and favorable energy band alignment. However, Cu_2O suffers from photocorrosion and chemical instability. Here, we present a novel approach utilizing a porous titanosilicate material (ETS-10) as a protective layer for Cu_2O, addressing these limitations. The Cu_2O was electrodeposited and coated with a thin ETS-10 layer, which prevents photocorrosion, enhances charge separation and transfer, and facilitates CO_2 capture through its highly porous structure. Comprehensive structural, compositional, and morphological analyses confirmed that ETS-10 effectively stabilized Cu_2O while maintaining its electronic properties (UV–Vis, XPS). The Cu_2O/ETS-10 photocathode exhibited a 25% enhancement in the photocurrent density at 0.0–0.1 V vs. RHE and significantly improved stability compared to bare Cu_2O. The thin ETS-10 layer acted as a passivation layer, improving charge transfer via tunneling mechanisms. This study introduces a multicomponent photocathode system, demonstrating a new application of ETS-10 in photoelectrochemical cells. The results highlight the potential of ETS-10 to enhance the efficiency and stability of photocathodes, offering a pathway for the design of advanced systems for solar-driven CO_2 reduction and artificial photosynthesis.

Keywords: photoelectrochemical reduction; copper(I) oxide; titanosilicate ETS-10; carbon dioxide conversion; methanol production; semiconductor photocathodes

check for updates

Academic Editors: Qiucheng Chen and Prabhakarn Arunachalam

Received: 27 December 2024
Revised: 15 March 2025
Accepted: 22 March 2025
Published: 26 March 2025

Citation: Szaniawska-Białas, E.; Parzuch, A.; Trinh, L.; Eliášová, P.; Solarska, R. Titanosilicate ETS-10-Modified Cu_2O for Enhanced Visible-Light Photoelectrochemical Activity. *Catalysts* **2025**, *15*, 313. https://doi.org/10.3390/catal15040313

Copyright: © 2025 by the authors. Licensee MDPI, Basel, Switzerland. This article is an open access article distributed under the terms and conditions of the Creative Commons Attribution (CC BY) license (https://creativecommons.org/licenses/by/4.0/).

1. Introduction

The continuously growing energy demands and the accelerating pace of climate change have brought the global community to a critical juncture, highlighting the urgent need for sustainable energy solutions and the effective mitigation of environmental challenges such as global warming and pollution. Among the most promising approaches to addressing these issues is the generation of alternative fuels through light-induced carbon dioxide (CO_2) reduction, which can play a pivotal role in both combating climate change and meeting the world's increasing energy needs. The concept of artificial photosynthesis offers a unique advantage by allowing solar energy to be stored as chemical compounds, such as methanol (CH_3OH), formic acid (HCOOH), or methane (CH_4), and by facilitating

these reactions under ambient conditions [1]. However, despite significant advancements in the development of photoelectrochemical (PEC) devices, these systems still face several challenges, including limited absorption efficiency, poor charge transfer, low durability, and high production costs [2,3]. Therefore, further improvements are necessary to design and fabricate widely applicable systems capable of efficient solar fuel production.

One potential solution to overcome these challenges is the use of *p*-type oxide semiconductors, which have a relatively small direct band gap, making them well suited for visible-light-driven CO_2 reduction [3,4]. Copper(I) oxide (Cu_2O) has gained significant attention due to its favorable band alignment, which positions its conduction and valence bands appropriately for efficient CO_2 reduction [5]. Additionally, Cu_2O promotes the formation of C1–C3 hydrocarbons and oxygenated products, which is strongly influenced by its crystallographic structure and anisotropic nature [6–10].

However, Cu_2O is prone to photocorrosion, as both the reduction and oxidation redox potentials of Cu_2O lie within its band gap, leading to its instability under light exposure. To mitigate this, various strategies have been explored to enhance the stability of copper(I) oxide-based photocathodes. One of the most effective approaches is the incorporation of protective layers, which can inhibit photocorrosion and improve the overall stability of the *p*-type semiconductor [3]. Protective coatings, such as n-type oxide semiconductors like titanium(IV) oxide (TiO_2), metal–organic frameworks, conducting polymers, and carbon-based materials, have been employed to enhance the performance of Cu_2O-based electrodes in light-induced CO_2 conversion reactions [4,11–16]. Studies on Cu_2O coated with TiO_2 have demonstrated significant improvements in both activity and stability when compared to bare Cu_2O [12,16,17]. The effectiveness of these coatings can depend on factors such as the material choice and the thickness of the protective layer, which can influence the charge transfer mechanisms within the photocathode system. For example, thinner coatings (<100 nm) may enable electron tunneling through the protective layer, potentially leading to the formation of heterojunctions, which can improve the photocathode performance.

Building on this knowledge, we propose the application of a thin titanosilicate layer, specifically Engelhard titanium silicate 10 (ETS-10), to protect the surface of Cu_2O from degradation while enhancing its photoelectrochemical performance. ETS-10, a porous material with octahedrally coordinated titanium, is known for its thermal and chemical stability. In addition to providing a protective coating, ETS-10's microporous structure can facilitate the selective conversion of molecules by accumulating substrates within its pores. This modification aims to exploit the unique properties of zeolites, such as molecular sieving, a large surface area, and its adsorption capacity, to improve the stability of Cu_2O while boosting its efficiency in photoelectrochemical processes [18,19].

In this study, we synthesized ETS-10 using a hydrothermal method and investigated the impact of this protective layer on the photoelectrochemical activity of Cu_2O. To the best of our knowledge, the use of ETS-10 as a protective layer for Cu_2O-based photocathodes for CO_2 reduction has not been explored previously. The proposed photocathode system, comprising Cu_2O protected by a thin layer of ETS-10, addresses the challenges of photocorrosion and enhances the material's photoelectrochemical activity. The interaction of ETS-10 with Cu_2O is expected to improve charge transfer and facilitate CO_2 capture within the porous structure of the titanosilicate. In this contribution, we present the physicochemical characterization of the materials and photocathode system, as well as an evaluation of the photoelectrochemical activity of the ETS-10-modified Cu_2O photocathode for CO_2 reduction. The results demonstrate that the Cu_2O/ETS-10 system exhibits an enhanced photocurrent density and improved stability compared to bare Cu_2O, with methanol identified as the primary product of the photoelectrochemical reduction of CO_2.

2. Results and Discussion

The crystallographic structure of the as-synthesized powder of titanosilicate material has been investigated by X-ray diffraction. The corresponding reflections at angles of 2θ equal to 6.05°, 12.33°, 24.8°, 25.9°, 27.3°, and 30.03° are characteristic of the ETS-10 material (Figure 1). The diffractogram shows mostly sharp and high-intensity peaks. The existence of broad peaks, especially at a low angle around 6°, may be related to structural defects in the ETS-10 framework. Thus, structural defects come from random intergrowths of two ideal polymorphs, which lead to stacking faults and titania sites exposed within the pores, and this has been widely discussed in the literature [20,21]. Moreover, the XRD pattern does not display the diffraction peaks characteristic of ETS-4 or the quartz phase, excluding the presence of impurities in the final product. Therefore, the utilization of P-25 as the titanium source allows us to obtain a pure ETS-10 material. The reason for this is probably the small particle size of P-25 (~0.03 μm) [22], which leads to the direct nucleation of the ETS-10 material [23,24]. The presented XRD results are consistent with the profiles reported in the literature [25]. Moreover, due to the fact that the structural porosity of the ETS-10 material might facilitate CO_2 capture in the proposed photocathode system, the texture properties of the ETS-10 material have been studied. The determined BET area of ETS-10 (216 m^2 g^{-1}) is around four times larger than that corresponding to commercial TiO_2 (55 m^2 g^{-1} Degussa P-25), commonly utilized as a coating layer in photoelectrochemical systems. Therefore, the introduction of an ETS-10 protective layer may increase the substrate concentration close to the active surface of the oxide semiconductor and improve the efficiency of the photoelectrochemical system.

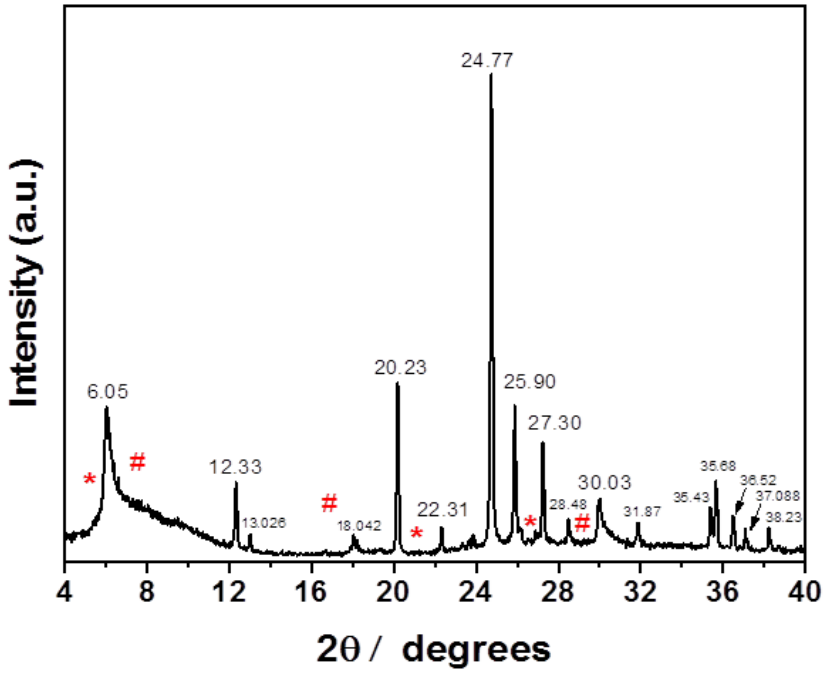

Figure 1. XRD patterns of titanosilicate ETS-10 material. Asterisks (*) and hashes (#) indicate secondary-phase quartz or ETS-4, respectively.

The structure and composition of the electrodeposited copper oxide layer on FTO before and after modification with the ETS-10 material have been characterized by X-ray powder diffraction (Figure 2) and supplemented with the results of X-ray photoelectron spectroscopy (Figure 3). Figure 2 shows the XRD patterns of (a) Cu_2O immobilized on FTO and covered with ETS-10 (FTO/Cu_2O/ETS-10), (b) pristine Cu_2O electrodeposited onto FTO glass (FTO/Cu_2O), and (c) bare fluorine-doped tin oxide (FTO). The diffraction

lines at 36.5°, 42.3°, 61.4°, and 73.6°, assigned to the (111), (200), (220), and (311) crystal planes, prove the formation of copper(I) oxide (Cu_2O, JCPDS ref. # 78-2076). Cu_2O crystals were mostly growing along the (111) and (200) planes, which enabled high photocatalytic activity and stability [8]. Diffraction peaks attributed to metallic copper (Cu, JCPDS ref. # 04-0836) and copper(II) oxide (CuO, JCPDS ref. # 05-0661) have not been observed. Although the presence of copper impurities, such as Cu and CuO, has not been confirmed by the XRD patterns, it cannot be unequivocally ruled out. However, the amount of copper traces may be considered negligible, if present. Moreover, the results obtained for pristine copper(I) oxide and the hybrid system containing copper(I) oxide and titanosilicate material confirmed that the sputtering deposition of the ETS-10 protective layer had no noticeable influence on the decomposition of Cu_2O. The diffraction peaks of tin oxide (SnO_2, JCPDS ref. # 41-1445) originated from fluorine-doped tin oxide (FTO)-coated glass, used as a conducting substrate in photocathode systems. Due to the broad diffraction lines located below 30°, reflecting the amorphous structure of the glass (FTO glass) and/or low material content, the crystal phase detection of ETS-10 immobilized on FTO was unsuccessful.

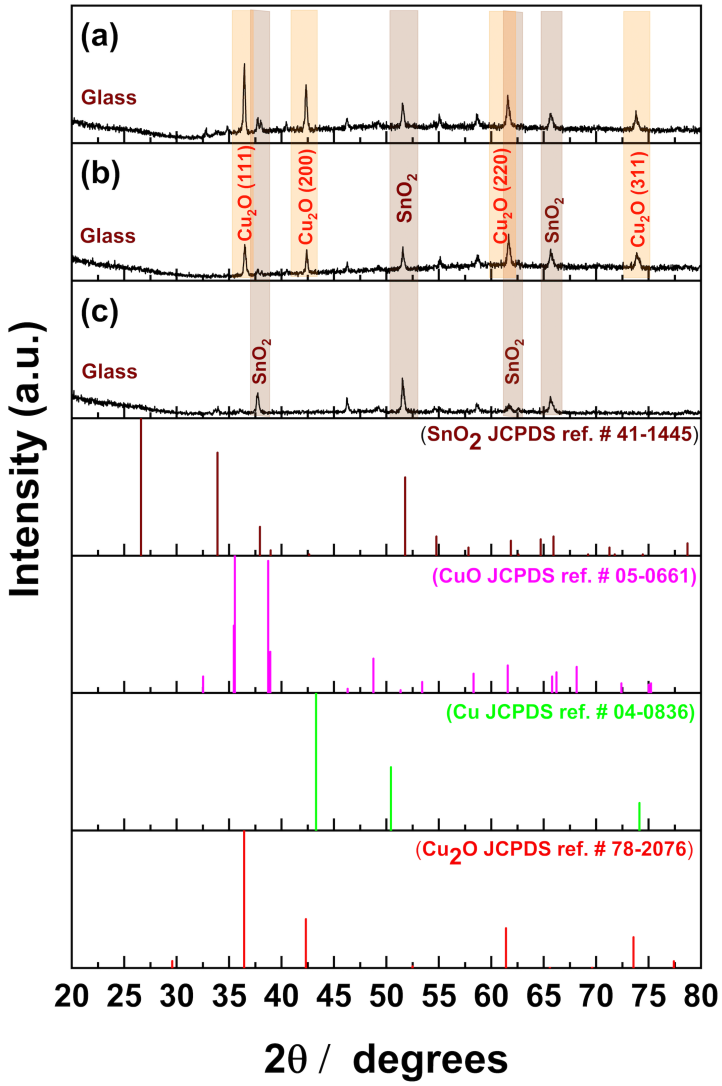

Figure 2. XRD patterns of (**a**) FTO/Cu_2O/ETS-10, (**b**) FTO/ Cu_2O, and (**c**) bare FTO. The standard data characteristics for Cu, CuO, Cu_2O, and SiO_2 as reference patterns have been included.

Therefore, to gain further insight into the structure and chemical state of the active layers of the proposed photocathode Cu_2O/ETS-10 system, an X-ray photoelectron spec-

troscopy analysis has been performed. The measurements were performed on two samples pre- and post-photoelectrochemical experiments to identify the changes in the chemical composition of the copper oxide active layer. All XPS spectra were charge-corrected to the adventitious C 1s peak at 284.6 eV. The presence of Cu, Ti, O, Si, and C elemental peaks was evident from the wide-range XPS survey spectra of both examined samples (Figure 3A,B). Figure 3C,D demonstrate the high-resolution spectra at the Cu 2p core level obtained for the Cu_2O/ETS-10 samples pre- and post-photoelectrochemical experiments, respectively. The Cu 2p spectra reveal two main peaks of Cu $2p_{3/2}$ and Cu $2p_{1/2}$ located at 932.7 eV and 952.5 eV, which can be assigned to Cu^+ or Cu^0 [26–28]. The binding energy separation of these two peaks was equal to 19.8 eV, which is consistent with the reported values for a pure metallic copper or copper(I) oxide [29]. Since the characteristic values of the binding energies for metallic Cu and Cu_2O differ slightly, a Cu LMM Auger examination was performed. The Auger peaks of copper(I) oxide appear at 916.8 eV, whereas, for metallic copper, they appear at 918.6 eV. The obtained experimental results excluded the existence of Cu^0 in both samples, namely pre- (Figure 3F) and post-photoelectrochemical experiments (Figure 3G), and are in a good agreement with the literature values [30,31]. However, the shake-up satellite peaks at a higher binding energy for Cu $2p_{3/2}$ and Cu $2p_{1/2}$, indicating the presence of an unfilled Cu $3d^9$ shell and thus the formation of $Cu(OH)_2$ and CuO at the surface of Cu_2O. The intensity of the Cu 2p shoulders and satellite peaks noticeably decreases with subsequent XPS measurements (Figure 3E), which indicates that the copper(II) impurities are located at the surface of the electrodeposited Cu_2O film and not within the bulk. Additionally, the results of XPS combined with XRD demonstrate that the content of copper(II) species (CuO, $Cu(OH)_2$) in the as-prepared photocathode is very low. Therefore, the presence of copper(II) oxide might be a result of the incipient oxidation of the sample surface in ambient air after synthesis, because CuO is the stable phase of copper oxide under these conditions [32]. Copper(II) hydroxide is highly probably a result of water absorption from air on the surface of copper oxides [33,34]. The deconvolution of the Cu 2p spectrum obtained for the Cu_2O/ETS-10 photocathode after the photoelectrochemical experiments indicates that the intensity of the peak attributed to copper(II) hydroxide significantly decreased, while the content of surface CuO only slightly increased (Figure 3D). Furthermore, Cu_2O is still the main phase of the copper oxide layer. The O 1s spectra of both Cu_2O/ETS-10 samples (as-prepared Figure 3H and post-photoelectrochemical experiments Figure 3I) can be deconvoluted into five main peaks located at 529.3, 530.3, 531.2, 531.7, and 532.7 eV. The first three peaks are attributed to oxygen atoms bonded to metal (CuO, Cu_2O/-Ti-O-Ti- and $Cu(OH)_2$), respectively [33,35,36]. The peak located at 531.7 eV is due to oxygen atoms in -Si-O-Ti- linkages, which occurs in the ETS-10 framework [35]. The last peak at 532.7 eV corresponds to water adsorbed on the surface of copper oxide [27,37]. Moreover, for the as-prepared Cu_2O/ETS-10 photocathode, an additional peak has been distinguished and assigned to CO_2/CO_3^{2-} species adsorbed on the surface of the metal oxide [36]. It is widely known that the exposure of a sample to ambient laboratory conditions leads to some amount of carbon contamination on its surface. The Ti 2p spectra are composed of two spin-orbital components, Ti $2p_{3/2}$ and Ti $2p_{1/2}$ (as-prepared sample Figure 3J and post-photoelectrochemical experiments Figure 3K). The former could be deconvoluted into three peaks located at 457.3, 458.5, and 459.6 eV. The binding energy of the Ti $2p_{3/2}$ core level centered at about 458.5 eV is attributed to the octahedrally coordinated Ti atoms in the ETS-10 framework [35]. The peak at 459.4 eV is assigned to the defects occurring within or at the exposed terminal ends of –O–Ti–O–Ti–O– chains in ETS-10 [35]. Additionally, the presence of small doublet peaks at 457.3 eV and 462.5 eV (split 5.2 eV) is related to Ti^{3+} species, but might also be caused by radiation damage during the XPS analysis [35]. Some peaks broaden or even shift with Ti in titanosilicates

in comparison to pure TiO_2, which could be explained by changes in the local structural configuration [38,39].

Therefore, based on the obtained XPS results, the main phase of the electrodeposited copper oxide layer was Cu_2O, which was sufficiently protected by a thin overlayer of ETS-10 titanosilicate against photocorrosion.

Upon acquiring the overall composition information, the morphology of the hybrid system of Cu_2O/ETS-10 was examined by scanning electron microscopy (Figure 4). The SEM image taken in the cross-section confirmed the presence of a thin ETS-10 coating on the Cu_2O surface (Figure 4A). The thickness of the ETS-10 titanosilicate layer was estimated at 100 nm. Therefore, it might be assumed that ETS-10 will play the role of a passivation layer to suppress charge recombination and the self-decomposition of the active semiconductor layer. In addition, the copper(I) oxide forms a continuous compact film consisting of octahedral crystals (Figure 4B). Studies conducted on the surfaces of photocatalysts have shown much higher photocatalytic activity for octahedral copper(I) oxide with exposed (111) faces than cubes [40]. The titanosilicate showed a truncated bipyramidal shape (red arrow) or platelet-shaped crystals (blue arrow) with tetragonal symmetry (Figure 4B), which is in agreement with the literature data [41–43].

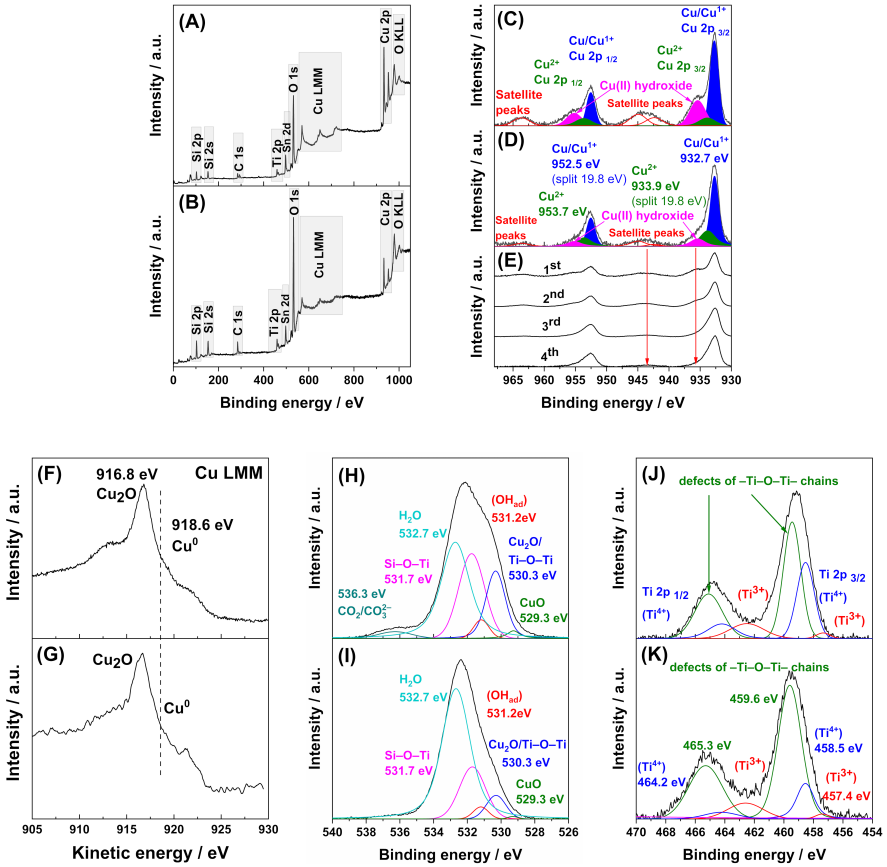

Figure 3. XPS spectra of FTO-supported ETS-10 zeolite-covered Cu_2O: full spectra of as-prepared sample (**A**) and post-photoelectrochemical experiments (**B**), Cu 2p spectra of as-prepared sample (**C**) and post-photoelectrochemical experiments (**D**), Cu 2p spectra of subsequent measurements for as-prepared sample (**E**), Cu LMM spectra of as-prepared (**F**) and post-photoelectrochemical experiments (**G**), O 1s spectra of as-prepared sample (**H**) and post-photoelectrochemical experiments (**I**), and Ti 2p spectra of as-prepared sample (**J**) and post-photoelectrochemical experiments (**K**).

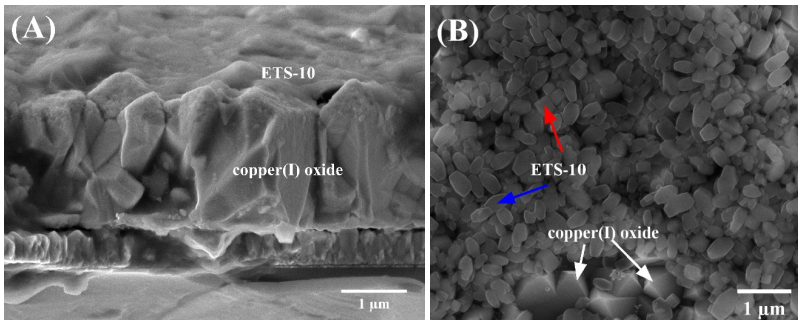

Figure 4. Cross-sectional (**A**) and top view (**B**) SEM images of zeolite-modified Cu_2O electrodeposited onto FTO.

Optical absorption behavior is one of the fundamental properties of materials/arrangements regarding their application in the photoelectrochemical field. Therefore, the UV–Vis diffuse reflectance spectra of the as-prepared materials/systems were analyzed in detail. Although the relevant photoelectrochemical measurements were performed under visible solar irradiation to fully characterize the active layers, the absorption measurements were performed in the UV–Vis range. Because FTO glass, as a conducting substrate, transmits incident light above a 300 nm wavelength and absorbs light in the UV spectrum, the diffuse reflectance measurements for the ETS-10 material were performed for an immobilized (Figure 5A, curve (a)) and powder (Figure 5A, curve (b)) form of the titanosilicate. Furthermore, Figure 5B shows electrodeposited Cu_2O on FTO glass substrates (Figure 5B, curve (a)) and copper(I) oxide immobilized onto FTO and covered with the ETS-10 porous material (Figure 5B, curve (b)). Pure copper(I) oxide, due to its low, direct band gap, has an absorption edge at ca. 650 nm. ETS-10 has a broad absorption band only in the UV range (200–350 nm) due to the presence of Ti^{4+} in octahedral coordination [44–46]. The band apparent at 250 nm is related to the Ti atoms bonded to four silica tetrahedrons present in the zeolite structure. The charge transfer within this framework is in a perpendicular direction in Ti-O-Ti-O chains, from Si- and Ti-linking oxygen atoms to the central titanium atom (Ti(IV)). The peak at 280 nm is assigned to charge transfer within the chain itself [43,47,48]. The presented UV–Vis spectra confirmed the ability of the FTO/Cu_2O/ETS-10 photocathode to adsorb in the visible range of the solar spectrum. Thus, the ETS-10 titanosilicate as a protective layer was not expected to diminish the performance of the *p*-type oxide semiconductor (Cu_2O) during photoelectrochemical carbon dioxide reduction. The band gap energy values were determined from the diffuse reflectance spectra by applying the Kubelka–Munk function and the Tauc plot. The relation can be expressed by the following Equation (1) [49–51]:

$$(F(R_\infty)h\nu)^n = B(h\nu - E_g) \quad (1)$$

where $R_\infty = R_{samples}/R_{standard}$ is the reflection of an infinitely thick specimen, $h\nu$ is the photon energy, B is a constant, E_g is the band gap, and the n factor depends on the nature of the electron transition and is either 1/2 or 2 for the indirect and direct transition band gaps, respectively. The modified Kubelka–Munk function was plotted as $(F(R)h\nu)^{1/n}$ versus $h\nu$ (Figure 6), enabling the extrapolation of the band gap energy. The value of n is usually determined from the best linear fit in the lower-energy absorption region of the plot; here, the value of 2 was used for both photocathode components. Therefore, for Cu_2O and the ETS-10 material, the band gap was estimated to be 2.01 eV and 3.84 eV, respectively (Figure 6). For bare copper(I) oxide, the band gap was approximated to be 2.05 eV, which differs slightly from the value obtained after protective layer deposition. The obtained figures are in agreement with the literature data [52]. Moreover, the utilization of the thin layer of the ETS-10 material did not alter the band position of copper(I) oxide. Therefore, it should be underlined that, due to the band edge positions, the role of the ETS-10 material

was limited to protecting copper(I) oxide, a *p*-type semiconductor, against (photo)corrosion under visible-light irradiation.

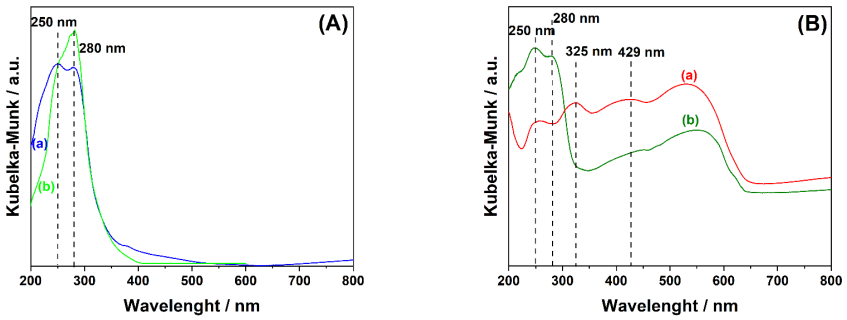

Figure 5. UV–Vis diffuse reflectance spectra of (**A**) ETS-10 sputtered onto FTO substrate (a) and ETS-10 in powder form (b). The analogous UV–Vis spectra of (**B**) bare Cu_2O (a) and ETS-10-modified Cu_2O layers prepared on FTO substrates together (b).

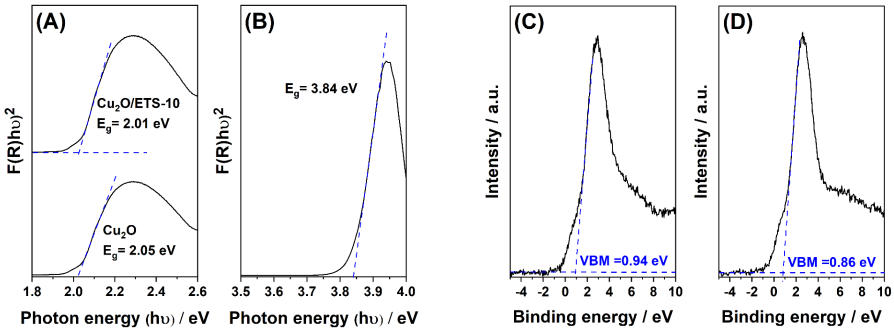

Figure 6. Kubelka–Munk plots of (**A**) ETS-10 and (**B**) Cu_2O deposited on FTO substrates. Low-intensity X-ray photoemission spectra for (**C**) Cu_2O and (**D**) Cu_2O coated with ETS-10.

By combining the results from UV–Vis diffuse reflectance spectroscopy with those of low-intensity X-ray photoemission spectroscopy, the electronic structure of copper(I) oxide in photocathode systems was determined. The valence band maximum (VBM) was estimated by applying the method of linear approximation to the leading edge of the XPS spectra to the baseline. The valence band edges of bare Cu_2O and Cu_2O modified with ETS-10 were determined to be 0.94 eV (vs. NHE) and 0.86 eV (vs. NHE) below the Fermi energy, respectively. Given that the band gaps of bare copper(I) oxide and copper(I) oxide modified with titanosilicate were 2.01 eV and 2.05 eV, the bottom of the conduction band should be located at 1.11 eV (2.05–0.94 eV) (vs. NHE) and 1.15 eV (2.01–0.86 eV) (vs. NHE), respectively. Thus, copper(I) oxide covered with a thin protective layer of ETS-10 possesses appropriate band edge positions for constant carbon dioxide reduction and/or water oxidation.

To measure the efficiency of the prepared hybrid photocathode and to determine the influence of the titanosilicate protective layer on charge carrier extraction, the incident photon-to-current efficiency (IPCE) was recorded (Figure 7). The conversion of incident photons to photocurrent as a function of the irradiation wavelength can be determined in the presence or absence of an external voltage. The IPCEs for bare Cu_2O and the multi-component system Cu_2O/ETS-10 were estimated from the following equation (Equation (2)):

$$IPCE = \frac{hc}{e} \times \frac{J_{ph}}{P_{mono} \times \lambda} = \frac{J_{ph}[\frac{\mathrm{mA}}{\mathrm{cm}^2}] \times 1239.8[\mathrm{V\ nm}]}{P_{mono}[\frac{\mathrm{mW}}{\mathrm{cm}^2}] \times \lambda[\mathrm{nm}]} \quad (2)$$

where h is Planck's constant, c is the speed of light, and e is the charge of electrons. J_{ph} is the photocurrent detected under the external voltage, P_{mono} is the power density, and λ is the wavelength of monochromatic light. It should be emphasized that, during the IPCE measurements, the light passed first through the front ETS-10 layer before reaching the Cu_2O absorber. In this configuration, the wider-band-gap ETS-10 (3.84 eV) absorbs photons at the high-energy end of the solar spectrum, while lower-energy photons pass through to be absorbed by Cu_2O (2.05 eV band gap) [53]. However, the IPCE values for Cu_2O/ETS-10 in the 350–475 nm range are nearly zero. This behavior is attributed to the optical properties of the ETS-10 protective layer, which predominantly absorbs photons in the UV range (200–350 nm). As a result, photons in the 350–475 nm range pass through the ETS-10 layer without significant absorption, allowing the underlying Cu_2O to absorb the incident photons. Nevertheless, the absorption efficiency of Cu_2O in this range is lower than in the UV region, leading to the observed low IPCE values in this spectral range. The IPCE curves show an improvement in the efficiency over most of the visible range of the solar spectrum when copper(I) oxide is coated with titanosilicate.

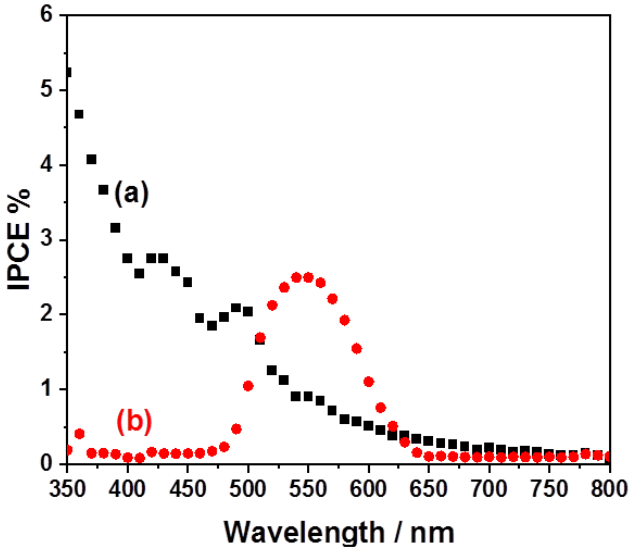

Figure 7. Photoaction spectra for the bare Cu_2O (a) and Cu_2O/ETS-10 (b) photocathode, recorded at 0.0 V vs. RHE in an Ar-saturated 0.1 mol dm^{-3} Na_2SO_4 solution.

The role of a thin protective ETS-10 layer on the photoelectrochemical performance towards the reduction of CO_2 might be described in comparison to bare Cu_2O. The low photostability and photoactivity of the FTO/Cu_2O photocathode due to both photodecomposition in aqueous media and fast photo-induced charge carrier recombination are shown in Figure 8A. To solve this problem, a passivation layer of ETS-10 is proposed (Figure 8B). The chopped cyclic voltammetry response of the FTO/Cu_2O/ETS-10 photocathode was measured in 0.1 mol dm^{-3} Na_2SO_4 electrolyte saturated with both argon and CO_2, respectively (Figure 8B). The obtained photocurrent density in the CO_2-saturated electrolyte was noticeably higher in comparison with the Ar-saturated solution across almost the entirety of the applied potential range (Figure 8B). This was attributed to the photoelectrochemical activity of the FTO/Cu_2O/ETS-10 cathode toward the reduction of carbon dioxide. The dark current of a hybrid material in both Ar- and CO_2-saturated solutions was low, which made the multi-component arrangement (Cu_2O/ETS-10) stable and resistant to decomposition in the potential range of interest (Figure 8B). Moreover, due to the very low current density, the electrochemical reduction of carbon dioxide on Cu_2O/ETS-10 in the applied potential range may be neglected. It should be emphasized that both photocathodes, i.e., bare copper(I) oxide and ETS-10-modified copper(I) oxide, are characterized by

good photoresponse properties. However, lower photocurrent spikes for multi-component systems indicate the more effective suppression of electron–hole recombination. In the photoelectrochemical reduction of carbon dioxide, the Cu_2O/ETS-10 photocathode exhibited highly enhanced photocurrents by about 25%, namely between 0.0 and 0.1 V vs. RHE, and showed improved stability in comparison to the bare copper(I) oxide electrode (Figure 8C). It seems that the potential of 0.1 V vs. RHE represents a compromise between the efficient reduction of carbon dioxide and competitive solar water splitting. Thus, the long-term photoelectrochemical measurement of the FTO/Cu_2O and FTO/Cu_2O/ETS-10 electrodes was performed at 0.1 V vs. RHE (Figure 8D). The pure stability of bare copper(I) oxide is visible in the significant decrease in the photocurrents over time, approaching values close to zero after half of the measurement time. Meanwhile, the ETS-10-modified copper(I) oxide shows visibly higher photocurrents even after 2 h of working, and the dark current shows an insignificant increase. Therefore, the thin protective layer of ETS-10 is expected to exhibit a stabilizing effect on Cu_2O during operation in an aqueous electrolyte. Finally, the bare titanosilicate material exhibited a negligible (photo)current density in the applied potential range, which is apparent from Figure 8E. Accordingly, the copper(I) oxide coated with a thin ETS-10 layer allowed the photoelectrochemical reduction of CO_2 under visible-light irradiation. The ETS-10 coating layer significantly decreased the direct contact of the electrolyte with the oxide semiconductor and simultaneously facilitated substrate (CO_2) accumulation close to the active surface of Cu_2O, due to the high capture capacity of the porous titanosilicate material. The fabrication of the thin coating layer allowed for the reduction of charge recombination at the surface states and improved simultaneous charge transfer across the semiconductor/electrolyte interface; it thus increased the efficiency of the photocatalyst, copper(I) oxide.

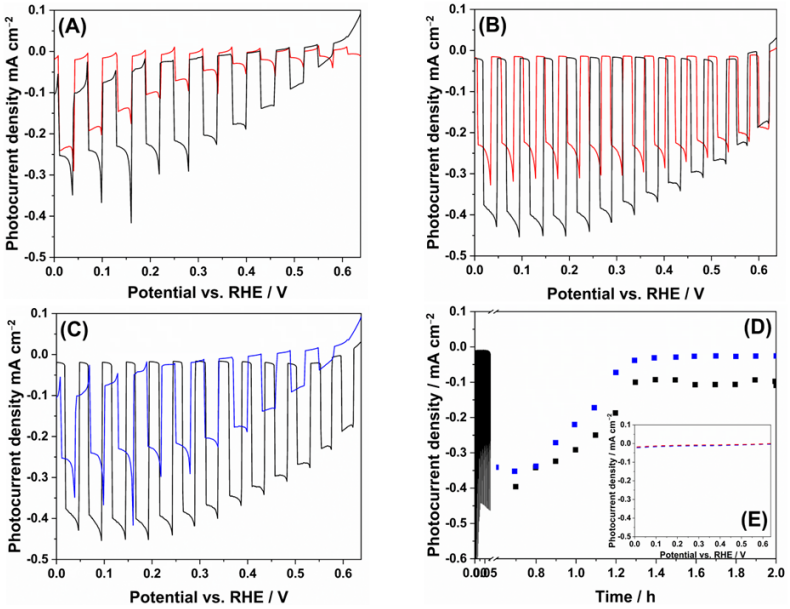

Figure 8. Plots of photocurrent vs. applied potential recorded for (**A**) bare Cu_2O and (**B**) ETS-10-modified Cu_2O photocathodes in 0.1 mol dm^{-3} sodium sulfate electrolyte saturated either with argon (red curve) or CO_2 (black curve). The pulsed responses were recorded upon illumination with chopped light. (**C**) Comparison of photoelectrochemical activity of FTO/Cu_2O (blue curve) and FTO/Cu_2O/ETS-10 (black curve) photocathode in CO_2-saturated 0.1 mol dm^{-3} sodium sulfate electrolyte. (**D**) The photocurrent stability at the imposed potential of 0.1 V vs. RHE for bare Cu_2O (blue symbol) and the ETS-10-modified Cu_2O (black symbol) photocathode. (**E**) The bottom inset illustrates the photoelectrochemical performance of the ETS-10 electrode measured in the dark (dash blue line) and under irradiation (dash red line) in 0.1 mol dm^{-3} sodium sulfate electrolyte saturated with CO_2.

Product Identification

In addition, some attention has also been paid to the identification of the reaction products. The appearance of methanol as the main product of the photoelectrochemical reduction of carbon dioxide on the FTO/Cu_2O/ETS-10 electrode has been confirmed by gas chromatography using a flame ionization detector (GC-FID). Comparative measurements with standard solutions of methanol, ethanol, and formic have been considered as well.

3. Experimental Section

3.1. Materials

Copper(II) sulfate pentahydrate ($CuSO_4 \cdot 5\,H_2O$, 98% Sigma-Aldrich, St. Louis, MO, USA), lactic acid ($CH_3CH(OH)CO_2H$, MW: 90.08 g/mol Sigma-Aldrich, MO, USA), sodium hydroxide (NaOH, 98.8% POCH BASIC, Gliwice, Poland), P-25 (TiO_2, 99.9% Acros Organics, Geel, Belgium), potassium fluoride (KF, ≥99.5% Sigma-Aldrich, MO, USA), a LudoxR AS-40 colloidal silica 40 wt.% suspension in H_2O (SiO_2, Sigma-Aldrich, MO, USA), and dimethylformamide (DMF, 99.8% Sigma-Aldrich, MO, USA) were used as the precursors for the preparation of the mixed working system. Sodium sulfate decahydrate ($Na_2SO_4 \cdot 10\,H_2O$, ACS reagent 99% from Sigma-Aldrich, MO, USA) saturated either with argon (Ar, 99.999% Air Products, Troy, MI, USA) or carbon dioxide (CO_2, 99.999% Air Products, MI, USA) was used as a supporting electrolyte for the reduction process. The electrolyte solutions were prepared with deionized water with resistivity of about 18 MΩ cm^{-1}.

Fluorine-doped tin oxide (FTO) conducting glass (resistivity, ∼8 Ω/sq; Sigma-Aldrich, MO, USA) was used as the photoelectrode substrate.

3.2. Copper(I) Oxide Electrodeposition

Copper(I) oxide was prepared via the electrodeposition technique on the fluorine-doped tin oxide (FTO)-covered glass, following a procedure described earlier [12,14]. The precursor solution for Cu_2O preparation was lactate-stabilized copper(II) sulfate, and electrochemical deposition was performed in a three-electrode configuration. The solution was obtained by the dissolution of 1.92 g of $CuSO_4$ and 6.71 mL of lactic acid in 30 mL of deionized water. The pH of the solution was maintained at pH = 9 by the controlled addition of solid sodium hydroxide. The cathodic deposition was carried out at a constant potential of −0.64 V vs. K_2SO_4-saturated Hg/Hg_2SO_4, the bath temperature was 60 °C, and the process was conducted for 30 min. The resulting copper(I) oxide film was left for 30 min at room temperature and later was subjected to calcination at 150 °C in air for 30 min.

3.3. Synthesis of Titanosilicate (ETS-10) as Protective Layer

ETS-10 was synthesized [54] hydrothermally from a gel with starting composition TiO_2:3 NaOH:0.74 KF:5SiO_2:68 H_2O. The initial step included the dispersion of 0.48 g of P-25 in water (H_2O; 7.4 g) by stirring. Next, 0.71 g of solid sodium hydroxide and 0.26 g of potassium fluoride were added to a constantly stirred solution of titanium(IV) oxide. After 30 min of stirring, 4.46 g of colloidal silica (40% silica, Aldrich, USA) was slowly added into the titania-containing solution. After combining the two mixtures, the solution was stirred for half an hour to obtain a homogeneous mixture. The pH value of the mixture was 10.4–10.5. Then, the gel was transferred into Teflon-lined autoclaves for dynamic crystallization at 230 °C for 44 h. The obtained product was isolated by centrifugation, washed three times by redispersing it into distilled water, and dried at 60 °C. Then, the synthesized ETS-10 zeolite was suspended in 10 mL of DMF and sprayed onto

electrodeposited copper(I) oxide. To avoid the undesirable influence of the solvent/organic residuals, the whole arrangement was calcinated at 150 °C for 30 min.

3.4. Characterization

3.4.1. XRD

X-ray powder diffraction (XRD) patterns were collected using a Bruker AXS D8 Advance diffractometer (Karlsruhe, Germany) equipped with a 1-D detector in the Bragg–Brentano geometry using CuKα (λ = 1.54056 Å) radiation operated at 30 mA and 40 kV. Data were collected in continuous mode over a 2θ range of 3–80°. The pristine ETS-10 sample was characterized in powder form using a standard PMMA (poly(methyl methacrylate)) XRD powder holder with a diameter of 25 mm and 1 mm depth. The copper(I) oxide film and multi-component arrangement were characterized after deposition on the FTO substrate.

N_2 adsorption/desorption measurements were carried out at −196 °C by using a Micromeritics 3Flex Volumetric Surface Area Analyzer (Norcross, Georgia). Before the measurements, the analyzed samples were outgassed under a turbomolecular pump vacuum using a Micromeritics Smart Vac Prep instrument. The procedure started at ambient temperature up to 110 °C, with a heating rate of 1 °C/min, until the residual pressure of 13.3 Pa was achieved. Then, the samples were pretreated under a vacuum at 250 °C (temperature ramp: 1 °C/min) for 8 h. The Brunauer–Emmett–Teller (BET) surface area was assessed using adsorption data in the relative pressure range of p/p_0 from 0.005 to 0.9. The t-plot method was applied to determine the micropore volume (V_{micro}). The adsorbed amount at p/p_0 = 0.95 determined the total pore volume (V_{total}). The pore volume was calculated by the Barrett–Joyner–Halenda (BJH) method.

3.4.2. XPS

The X-ray photoelectron spectroscopy (XPS) experiments were performed at Charles University, in the Faculty of Mathematics and Physics, in Prague, using an ultra-high vacuum surface analytical system with a non-monochromatic Al Kα X-ray source (1486.6 eV), operated at 12.5 kV and 20 mA. The source power was maintained at 250 W. The energy analyzer was the SPECS Phoibos 150 (Berlin, Germany), equipped with an MCD-9 detector (Berlin, Germany). The system base pressure was 10-8 Pa. The survey spectra were collected with a pass energy of 40 eV, step size of 0.5 eV, and dwell time of 100 ms. The core-level spectra of Cu LMM, Cu 2*p*, O 1*s*, Ti 2*p*, and C 1*s* were collected with a pass energy of 20 eV, step size of 0.05 eV, and dwell time of 100 ms. All photoemission spectra were fitted with a mixture of Lorentzian and Gaussian function profiles after Shirley background subtraction.

3.4.3. SEM/EDS

The morphologies of the produced arrangement Cu_2O/ETS-10 were analyzed with the use of scanning electron microscopy (SEM) on a Zeiss Sigma HV microscope (Oberkocken, Germany), equipped with an InLens detector at the Faculty of Physics, University of Warsaw, and with the JEOL IT-800 HR-SEM using a secondary electron (SE) detector (Akishima, Japan) at the Facility of Biology Section, Faculty of Science (IMCF Vinicna). The energy-dispersive X-ray spectroscopy (EDS) system was used to obtain the elemental analysis information.

3.4.4. UV–Vis Diffuse Reflectance

The diffuse reflectance spectra were collected in the UV–Vis region using a double-beam UV–Vis spectrophotometer equipped with a photomultiplier tub detector (JASCO V-650) (Tokyo, Japan). Light with a 200–800 nm wavelength was generated with halogen and deuterium lamps.

3.4.5. Photoelectrochemical Measurements

The experimental setup for the photoelectrochemical experiments included a light source–solar simulator (Newport-81094 Model equipped with a 150 W Xe lamp and an AM 1.5 Global (2 × 2 inch) filter) (Newport International, Inc., Arlington, TX, USA), a potentiostat, a CH Instruments (Austin, TX, USA) 660D workstation, and a two-compartment cell. The cathodic compartment was physically separated from the anodic one by a proton exchange membrane (Nafion 117; thickness, 0.007 inches). The three-electrode system consisted of a working electrode, where FTO was utilized in a glass substrate (geometric areas, 0.5 cm^2), a Pt wire was applied as a counter electrode, and the reference electrode was a mercury sulfate electrode (Hg/Hg_2SO_4/sat. K_2SO_4). Unless otherwise stated, all potentials were converted to the reversible hydrogen electrode (RHE) reference scale. The aqueous electrolyte solutions used were 0.1 mol dm^{-3} Na_2SO_4, having pH = 6.4 when saturated with argon and pH = 5.3 when CO_2 was bubbled through the cell. The solutions were saturated with inert gas or carbon dioxide by bubbling the gases through the cell for 20 min before and during the measurements (above the solution in the latter case). The photocurrent vs. potential curves were measured with a potential sweep of 10 mV s^{-1} in the potential range of 0.64 to 0.0 V vs. RHE. During the measurements, the light intensity was adjusted to 100 mW cm^{-2} with a calibrated reference cell (Portable Radiometer, International Light Technologies Model 1400 with SEL623 (International Light Technologies INC, Gaithersburg, MA, USA) and a thermopile detector with NIST Traceable Calibration (the National Institute of Standards and Technology, Gaithersburg, MD, USA)). Photoresponses were measured in both continuous and chopper modes.

Incident photon-to-electron conversion efficiency (IPCE) measurements were performed on a Newport Quantum Efficiency Measurement System (Newport International, Inc., Arlington, TX, USA) in a single-compartment, three-electrode quartz electrochemical cell. The wavelength range was 350–800 nm ($\Delta\lambda$ = 10 nm step size). The IPCE profiles were recorded at E = 0.0 V vs. RHE, in an Ar-saturated 0.1 mol dm^{-3} Na_2SO_4 solution.

Electrochemical impedance spectra (EIS) were recorded at open circuit potential under dark and light conditions in the 0.1 Hz to 0.1 MHz frequency range, with the AC amplitude of 10 mV.

3.4.6. Product Identification

The products of photoelectrochemical carbon dioxide reduction were identified using gas chromatography (GC) coupled with a flame ionization detector (FID) to detect hydrocarbons and a thermal conductivity detector (TCD) to detect H_2, O_2, CO (Figure 9). The photoelectrochemical experiment was performed for 2 h, and, after this, the reaction product was monitored. The headspace sampling approach was used for the direct analysis of both volatile compounds and liquid products. A gaseous sample from the headspace of the cathodic compartment was manually extracted using a 1.0 mL airtight syringe and introduced into the GC-TCD. Furthermore, a liquid product analysis was performed. Four samples, each containing 2 mL of the electrolyte solution after long-term photoelectrochemical CO_2 reduction measurements, were taken in glass vials. The glass vials were sealed with a septum and heated in a water bath at 75–80 °C for 30 min. Next, a gaseous sample from the headspace of the vial was manually extracted using a 1.0 ml airtight syringe and introduced into the GC-FID. The liquid product analysis was preceded by heating the shut vial at 75–80 °C in a water bath for 30 min. The gaseous sample containing products was injected by using an airtight syringe. The GC-FID was equipped with an HP-5 (30 m length, 0.25 μm thickness, 0.32 mm inner diameter) column, and it was set at 45 °C. Nitrogen was used as the carrier gas during the measurements. The GC-TCD was equipped with a

CP7429 column (Shimadzu, Kyoto, Japan), and it was set at 45 °C. Helium was used as the GC carrier gas. Both the FID and TCD instruments were adjusted to 250 °C.

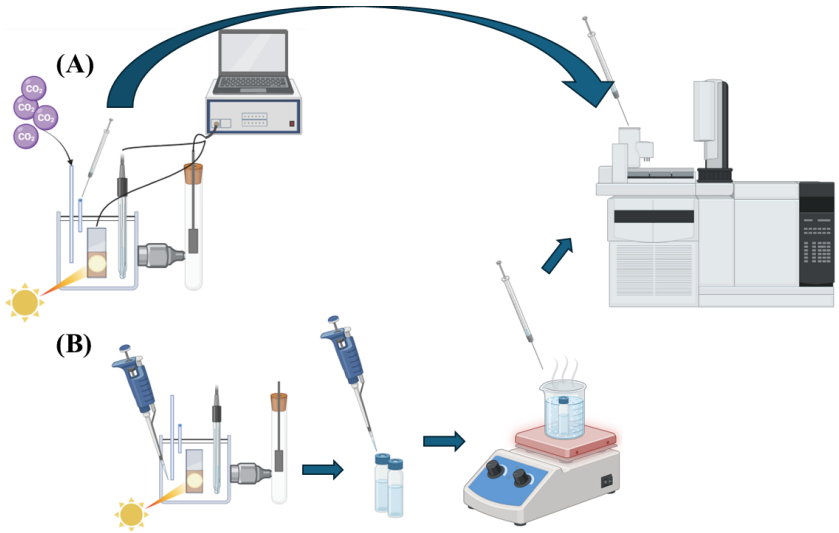

Figure 9. The photoelectrochemical reactor and the product detection setup. (**A**) Analysis of a gaseous sample from the headspace of the cathodic compartment. (**B**) Liquid product analysis obtained after long-term photoelectrochemical performance. Created with BioRender software (https://www.biorender.com/, BioRender, Canada)

4. Conclusions

In this study, a novel photocathode system comprising copper(I) oxide (Cu_2O) coated with a thin protective layer of titanosilicate ETS-10 was successfully designed, fabricated, and characterized for the photoelectrochemical reduction of carbon dioxide (CO_2) under visible-light irradiation. The ETS-10 material demonstrated a dual role as a protective layer and an enhancement agent, providing significant advantages in terms of stability, selectivity, and photocatalytic performance.

The characterization of the hybrid Cu_2O/ETS-10 system confirmed that the ETS-10 layer effectively protected the Cu_2O against photocorrosion while preserving the semiconductor's favorable electronic structure. Moreover, the porous structure of ETS-10 facilitated the adsorption and accumulation of CO_2 near the active surface, thereby enhancing the photoelectrochemical reduction efficiency. The system exhibited a 25% increase in the photocurrent density and improved stability compared to bare Cu_2O, addressing the common challenges of photocathode degradation and charge carrier recombination.

The product analysis confirmed the formation of methanol as the primary product of CO_2 reduction, highlighting the system's potential for producing valuable chemicals. The results demonstrate that the combination of Cu_2O with ETS-10 offers a promising approach to achieving efficient, stable, and selective photoelectrochemical systems for solar-driven fuel production.

This work provides a new pathway for the development of advanced photocathodes using tailored protective layers, paving the way for sustainable energy solutions through artificial photosynthesis. Future research may explore the optimization of the material properties, scaling up the system, and expanding its application to other photocatalytic processes.

Author Contributions: Conceptualization, E.S.-B.; methodology, E.S.-B. and R.S.; validation, E.S.-B. and A.P.; formal analysis, E.S.-B. and A.P.; investigation, E.S.-B.; resources, R.S.; data curation, E.S.-B.; writing—original draft preparation, E.S.-B.; writing—review and editing, E.S.-B., R.S., L.T., P.E. and

A.P.; visualization, E.S.-B. and L.T.; supervision, R.S.; project administration, R.S.; funding acquisition, R.S. All authors have read and agreed to the published version of the manuscript.

Funding: This research was funded by the National Centre for Research and Development, POLNOR Program, grant number HERA 0043/2019, and the National Science Centre Poland (NCN) through SONATA Bis project 2017/26/E/ST5/01137 SONATA BIS NCN awarded to R.S. The research was also funded by the EU within Horizon Europe Research—DESIRED project (project code: 101083355).

Data Availability Statement: The data presented in this study are available on request from the corresponding author. The data are not publicly available due to institutional policies.

Acknowledgments: The authors thank the Laboratory of Electron Microscopy, Imaging Methods Core Facility of Biology Section, Faculty of Science (IMCF Vinicna), Charles University, for the SEM images. The authors also thank Xiaohui Ju from the Department of Surface and Plasma Science, Faculty of Mathematics and Physics, Charles University, for the XPS measurements.

Conflicts of Interest: The authors declare no conflicts of interest.

References

1. Yoshino, S.; Takayama, T.; Yamaguchi, Y.; Iwase, A.; Kudo, A. CO_2 Reduction Using Water as an Electron Donor over Heterogeneous Photocatalysts Aiming at Artificial Photosynthesis. *Accounts Chem. Res.* **2022**, *55*, 966–977. [CrossRef]
2. Kumaravel, V.; Bartlett, J.; Pillai, S.C. Photoelectrochemical Conversion of Carbon Dioxide (CO_2) into Fuels and Value-Added Products. *ACS Energy Lett.* **2020**, *5*, 486–519. [CrossRef]
3. Tang, B.; Xiao, F.X. An Overview of Solar-Driven Photoelectrochemical CO_2 Conversion to Chemical Fuels. *ACS Catal.* **2022**, *12*, 9023–9057. [CrossRef]
4. Kecsenovity, E.; Endrődi, B.; Tóth, P.S.; Zou, Y.; Dryfe, R.A.; Rajeshwar, K.; Janáky, C. Enhanced Photoelectrochemical Performance of Cuprous Oxide/Graphene Nanohybrids. *J. Am. Chem. Soc.* **2017**, *139*, 6682–6692. [CrossRef]
5. Baran, T.; Visibile, A.; Busch, M.; He, X.; Wojtyla, S.; Rondinini, S.; Minguzzi, A.; Vertova, A. Copper Oxide-Based Photocatalysts and Photocathodes: Fundamentals and Recent Advances. *Molecules* **2021**, *26*, 7271. [CrossRef] [PubMed]
6. Xu, X.; Gao, Z.; Cui, Z.; Liang, Y.; Li, Z.; Zhu, S.; Yang, X.; Ma, J. Synthesis of Cu_2O Octadecahedron/TiO_2 Quantum Dot Heterojunctions with High Visible Light Photocatalytic Activity and High Stability. *ACS Appl. Mater. Interfaces* **2016**, *8*, 91–101. [CrossRef]
7. Janáky, C.; Hursán, D.; Endrődi, B.; Chanmanee, W.; Roy, D.; Liu, D.; De Tacconi, N.R.; Dennis, B.H.; Rajeshwar, K. Electro- and Photoreduction of Carbon Dioxide: The Twain Shall Meet at Copper Oxide/Copper Interfaces. *ACS Energy Lett.* **2016**, *1*, 332–338. [CrossRef]
8. Zheng, Z.; Huang, B.; Wang, Z.; Guo, M.; Qin, X.; Zhang, X.; Wang, P.; Dai, Y. Crystal faces of Cu_2O and their stabilities in photocatalytic reactions. *J. Phys. Chem. C* **2009**, *113*, 14448–14453. [CrossRef]
9. Siegfried, M.J.; Choi, K.S. Elucidating the effect of additives on the growth and stability of Cu_2O surfaces via shape transformation of pre-grown crystals. *J. Am. Chem. Soc.* **2006**, *128*, 10356–10357. [CrossRef]
10. Soon, A.; Todorova, M.; Delley, B.; Stampfl, C. Thermodynamic stability and structure of copper oxide surfaces: A first-principles investigation. *Phys. Rev. B Condens. Matter Mater. Phys.* **2007**, *75*, 125420. [CrossRef]
11. Luo, J.; Steier, L.; Son, M.K.; Schreier, M.; Mayer, M.T.; Grätzel, M. Cu_2O Nanowire Photocathodes for Efficient and Durable Solar Water Splitting. *Nano Lett.* **2016**, *16*, 1848–1857. [CrossRef] [PubMed]
12. Szaniawska, E.; Bienkowski, K.; Rutkowska, I.A.; Kulesza, P.J.; Solarska, R. Enhanced photoelectrochemical CO_2-reduction system based on mixed Cu_2O–nonstoichiometric TiO_2 photocathode. *Catal. Today* **2018**, *300*, 145–151. [CrossRef]
13. Deng, X.; Li, R.; Wu, S.; Wang, L.; Hu, J.; Ma, J.; Jiang, W.; Zhang, N.; Zheng, X.; Gao, C.; et al. Metal-Organic Framework Coating Enhances the Performance of Cu_2O in Photoelectrochemical CO_2 Reduction. *J. Am. Chem. Soc.* **2019**, *141*, 10924–10929. [CrossRef] [PubMed]
14. Szaniawska, E.; Rutkowska, I.A.; Frik, M.; Wadas, A.; Seta, E.; Krogul-Sobczak, A.; Rajeshwar, K.; Kulesza, P.J. Reduction of carbon dioxide at copper(I) oxide photocathode activated and stabilized by over-coating with oligoaniline. *Electrochim. Acta* **2018**, *265*, 400–410. [CrossRef]
15. Szaniawska, E.; Rutkowska, I.A.; Seta, E.; Tallo, I.; Lust, E.; Kulesza, P.J. Photoelectrochemical reduction of CO_2: Stabilization and enhancement of activity of copper(I) oxide semiconductor by over-coating with tungsten carbide and carbide-derived carbons. *Electrochim. Acta* **2020**, *341*, 136054. [CrossRef]
16. Akbar, M.B.; Gong, Y.; Wang, Y.; Woldu, A.R.; Zhang, X.; He, T. Role of TiO_2 coating layer on the performance of Cu_2O photocathode in photoelectrochemical CO_2 reduction. *Nanotechnology* **2021**, *32*, 395707. [CrossRef]

17. Aguirre, M.E.; Zhou, R.; Eugene, A.J.; Guzman, M.I.; Grela, M.A. Cu_2O/TiO_2 heterostructures for CO_2 reduction through a direct Z-scheme: Protecting Cu_2O from photocorrosion. *Appl. Catal. B Environ.* **2017**, *217*, 485–493. [CrossRef]
18. Suib, S.L.; Přech, J.; Čejka, J.; Kuwahara, Y.; Mori, K.; Yamashita, H. Some novel porous materials for selective catalytic oxidations. *Mater. Today* **2020**, *32*, 244–259. [CrossRef]
19. Barrocas, B.T.; Přech, J.; Filip Edelmannová, M.; Szaniawska, E.; Kočí, K.; Čejka, J. Titanosilicates enhance carbon dioxide photocatalytic reduction. *Appl. Mater. Today* **2022**, *26*, 101392. [CrossRef]
20. Krisnandi, Y.K.; Southon, P.D.; Adesina, A.A.; Howe, R.F. ETS-10 as a photocatalyst. *Int. J. Photoenergy* **2003**, *5*, 131–140. [CrossRef]
21. Anderson, M.W.; Terasaki, O.; Ohsuna, T.; Philippou, A.; MacKay, S.P.; Ferreira, A.; Rocha, J.; Lidin, S. Structure of the microporous titanosilicate ETS-10. *Nature* **1994**, *367*, 347–351. [CrossRef]
22. Melcher, J.; Feroz, S.; Bahnemann, D. Comparing photocatalytic activities of commercially available iron-doped and iron-undoped aeroxide TiO_2 P25 powders. *J. Mater. Sci.* **2017**, *52*, 6341–6348. [CrossRef]
23. Krisnandi, Y.K.; Lachowski, E.E.; Howe, R.F. Effects of Ion Exchange on the Structure of ETS-10. *ChemInform* **2006**, *37*, 928–933. [CrossRef]
24. Lv, L.; Su, F.; Zhao, X.S. A reinforced study on the synthesis of microporous titanosilicate ETS-10. *Microporous Mesoporous Mater.* **2004**, *76*, 113–122. [CrossRef]
25. Zaheer, M.A.; Poppitz, D.; Feyzullayeva, K.; Wenzel, M.; Matysik, J.; Ljupkovic, R.; Zarubica, A.; Karavaev, A.A.; Pöppl, A.; Gläser, R.; et al. Synthesis of highly active ETS-10-based titanosilicate for heterogeneously catalyzed transesterification of triglycerides. *Beilstein J. Nanotechnol.* **2019**, *10*, 2039–2061. [CrossRef]
26. Bojestig, E.; Cao, Y.; Nyborg, L. Surface chemical analysis of copper powder used in additive manufacturing. *Surf. Interface Anal.* **2020**, *52*, 1104–1110. [CrossRef]
27. Biesinger, M.C.; Lau, L.W.; Gerson, A.R.; Smart, R.S.C. Resolving surface chemical states in XPS analysis of first row transition metals, oxides and hydroxides: Sc, Ti, V, Cu and Zn. *Appl. Surf. Sci.* **2010**, *257*, 887–898. [CrossRef]
28. Wang, Q.; Zhang, Y.; Liu, Y.; Wang, K.; Qiu, W.; Chen, L.; Li, W.; Li, J. Photocorrosion behavior of Cu_2O nanowires during photoelectrochemical CO_2 reduction. *J. Electroanal. Chem.* **2022**, *912*, 116252. [CrossRef]
29. Pauly, N.; Tougaard, S.; Yubero, F. Determination of the Cu 2p primary excitation spectra for Cu, Cu_2O and CuO. *Surf. Sci.* **2014**, *620*, 17–22. [CrossRef]
30. Iijima, Y.; Niimura, N.; Hiraoka, K. Prevention of the reduction of CuO during X-ray photoelectron spectroscopy analysis. *Surf. Interface Anal.* **1996**, *24*, 193–197. [CrossRef]
31. Poulston, S.; Parlett, P.M.; Stone, P.; Bowker, M. Surface oxidation and reduction of CuO and Cu_2O studied using XPS and XAES. *Surf. Interface Anal.* **1996**, *24*, 811–820. [CrossRef]
32. Wilson, S.S.; Bosco, J.P.; Tolstova, Y.; Scanlon, D.O.; Watson, G.W.; Atwater, H.A. Interface stoichiometry control to improve device voltage and modify band alignment in ZnO/Cu_2O heterojunction solar cells. *Energy Environ. Sci.* **2014**, *7*, 3606–3610. [CrossRef]
33. Zhu, C.; Osherov, A.; Panzer, M.J. Surface chemistry of electrodeposited Cu_2O films studied by XPS. *Electrochim. Acta* **2013**, *111*, 771–778. [CrossRef]
34. Baklanov, M.R.; Shamiryan, D.G.; Tökei, Z.; Beyer, G.P.; Conard, T.; Vanhaelemeersch, S.; Maex, K. Characterization of Cu surface cleaning by hydrogen plasma. *J. Vac. Sci. Technol. B Microelectron. Nanometer Struct. Process. Meas. Phenom.* **2001**, *19*, 1201–1211. [CrossRef]
35. Lv, L.; Lee, F.Y.; Zhou, J.; Su, F.; Zhao, X.S. XPS study on microporous titanosilicate ETS-10 upon acid treatment. *Microporous Mesoporous Mater.* **2006**, *96*, 270–275. [CrossRef]
36. Trinh, Q.T.; Bhola, K.; Amaniampong, P.N.; Jérôme, F.; Mushrif, S.H. Synergistic Application of XPS and DFT to Investigate Metal Oxide Surface Catalysis. *J. Phys. Chem. C* **2018**, *122*, 22397–22406. [CrossRef]
37. McIntyre, N.S.; Sunder, S.; Shoesmith, D.W.; Stanchell, F.W. Chemical Information From Xps—Applications To the Analysis of Electrode Surfaces. *J. Vac. Sci. Technol.* **1980**, *18*, 714–721. [CrossRef]
38. Manangon-Perugachi, L.E.; Smeets, V.; Vivian, A.; Kainthla, I.; Eloy, P.; Aprile, C.; Debecker, D.P.; Gaigneaux, E.M. Mesoporous methyl-functionalized titanosilicate produced by aerosol process for the catalytic epoxidation of olefins. *Catalysts* **2021**, *11*, 196. [CrossRef]
39. Su, Y.; Balmer, M.L.; Bunker, B.C. Raman spectroscopic studies of silicotitanates. *J. Phys. Chem. B* **2000**, *104*, 8160–8169. [CrossRef]
40. Xu, H.; Wang, W.; Zhu, W. Shape evolution and size-controllable synthesis of Cu_2O octahedra and their morphology-dependent photocatalytic properties. *J. Phys. Chem. B* **2006**, *110*, 13829–13834. [CrossRef]
41. Anderson, M.W.; Terasaki, O.; Ohsuna, T.; Malley, P.J.O.; Philippou, A.; Mackay, S.P.; Ferreira, A.; Rocha, J.; Lidin, S. Microporous titanosilicate ETS-10: A structural survey. *Philos. Mag. B* **1995**, *71*, 813–841. [CrossRef]
42. Kuzyaka, D.; Galioglu, S.; Altın, I.; Sokmen, M.; Akata, B. The effect of microporous vanadosilicate AM-6 thin films as photocatalysts for the degradation of methylene blue. *J. Photochem. Photobiol. A Chem.* **2018**, *366*, 127–135. [CrossRef]
43. Ng, Y.C.; Jei, C.Y.; Shamsuddin, M. Titanosilicate ETS-10 derived from rice husk ash. *Microporous Mesoporous Mater.* **2009**, *122*, 195–200. [CrossRef]

44. Galioğlu, S.; Zahmakiran, M.; Eren Kalay, Y.; Özkar, S.; Akata, B. Effect of silver encapsulation on the local structure of titanosilicate ETS-10. *Microporous Mesoporous Mater.* **2012**, *159*, 1–8. [CrossRef]
45. Das, T.K.; Chandwadkar, A.J.; Budhkar, A.P.; Belhekar, A.A.; Sivasanker, S. Studies on the synthesis of ETS-10 I. Influence of synthesis parameters and seed content. *Microporous Mater.* **1995**, *4*, 195–203. [CrossRef]
46. Suib, S.L.; Přech, J.; Szaniawska, E.; Čejka, J. Recent Advances in Tetra- (Ti, Sn, Zr, Hf) and Pentavalent (Nb, V, Ta) Metal-Substituted Molecular Sieve Catalysis. *Chem. Rev.* **2023**, *123*, 877–917. [CrossRef]
47. Liepold, A.; Roos, K.; Reschetilowski, W.; Lin, Z.; Rocha, J.; Philippou, A.; Anderson, M.W. Characterisation studies on the new microporous aluminium-containing ETS-10 molecular sieve used for processing larger molecules. *Microporous Mater.* **1997**, *10*, 211–224. [CrossRef]
48. Philippou, A.; Anderson, M.W. Aldol-type reactions over basic microporous titanosilicate ETS-10 type catalysts. *J. Catal.* **2000**, *189*, 395–400. [CrossRef]
49. Makuła, P.; Pacia, M.; Macyk, W. How To Correctly Determine the Band Gap Energy of Modified Semiconductor Photocatalysts Based on UV-Vis Spectra. *J. Phys. Chem. Lett.* **2018**, *9*, 6814–6817. [CrossRef]
50. López, R.; Gómez, R. Band-gap energy estimation from diffuse reflectance measurements on sol–gel and commercial TiO_2: A comparative study. *J. Sol-Gel Sci. Technol.* **2012**, *61*, 1–7. [CrossRef]
51. Nowak, M.; Kauch, B.; Szperlich, P. Determination of energy band gap of nanocrystalline SbSI using diffuse reflectance spectroscopy. *Rev. Sci. Instrum.* **2009**, *80*, 046107. [CrossRef] [PubMed]
52. Borello, E.; Lamberti, C.; Bordiga, S.; Zecchina, A.; Areán, C.O. Quantum-size effects in the titanosilicate molecular sieve. *Appl. Phys. Lett.* **1997**, *71*, 2319–2321. [CrossRef]
53. Pan, L.; Kim, J.H.; Mayer, M.T.; Son, M.K.; Ummadisingu, A.; Lee, J.S.; Hagfeldt, A.; Luo, J.; Grätzel, M. Boosting the performance of Cu_2O photocathodes for unassisted solar water splitting devices. *Nat. Catal.* **2018**, *1*, 412–420. [CrossRef]
54. Liu, X.; Thomas, J.K. Synthesis of microporous titanosilicates ETS-10 and ETS-4 using solid TiO_2 as the source of titanium. *Chem. Commun.* **1996**, 1435–1436. . [CrossRef]

Disclaimer/Publisher's Note: The statements, opinions and data contained in all publications are solely those of the individual author(s) and contributor(s) and not of MDPI and/or the editor(s). MDPI and/or the editor(s) disclaim responsibility for any injury to people or property resulting from any ideas, methods, instructions or products referred to in the content.